AFRL-OSR-VA-TR-2014-0321

Dynamic Chemical and Structural Changes of Heterogeneous Catalysts

Robert Rioux
PENNSYLVANIA STATE UNIVERSITY

11/26/2014
Final Report

Air Force Research Laboratory
AF Office Of Scientific Research (AFOSR)/ RTE
Arlington, Virginia 22203
Air Force Materiel Command

REPORT DOCUMENTATION PAGE

Form Approved
OMB No. 0704-0188

1. REPORT DATE *(DD-MM-YYYY)*	**2. REPORT TYPE**	**3. DATES COVERED** *(From - To)*
11-10-2014	Final Report	4/15/2012 – 10/14/2014

4. TITLE AND SUBTITLE

Dynamic Chemical and Structural Changes of Heterogeneous Catalysts Observed in Real Time: From Catalysis-Induced Fluxionality to Catalytic Cycles

5a. CONTRACT NUMBER

5b. GRANT NUMBER
FA9550-12-1-0204

5c. PROGRAM ELEMENT NUMBER

6. AUTHOR(S)

Robert M Rioux

5d. PROJECT NUMBER

5e. TASK NUMBER

5f. WORK UNIT NUMBER

7. PERFORMING ORGANIZATION NAME(S) AND ADDRESS(ES)

Pennsylvania State University
408 OLD MAIN
UNIVERSITY PARK PA 16802-1505

8. PERFORMING ORGANIZATION REPORT NUMBER

9. SPONSORING / MONITORING AGENCY NAME(S) AND ADDRESS(ES)

USAF, AFRL DUNS 143574726
AF OFFICE OF SCIENTIFIC RESEARCH
875 N. RANDOLPH ST. ROOM 3112
ARLINGTON VA 22203

10. SPONSOR/MONITOR'S ACRONYM(S)

11. SPONSOR/MONITOR'S REPORT NUMBER(S)

12. DISTRIBUTION / AVAILABILITY STATEMENT

13. SUPPLEMENTARY NOTES

14. ABSTRACT

The results from "Dynamic Chemical and Structural Changes of Heterogeneous Catalysts Observed in Real Time: From Catalysis-Induced Fluxionality to Catalytic Cycles" have been summarized including (1) construction/evaluation of a transmission infrared spectroscopy cell utilizing either a pulsed valve or laser to generate temporal perturbation that enables millisecond to microsecond time resolution; (2) millisecond-wide pulses to titrate kink, step and terrace sites, followed by their removal with pulsed hydrogen in order to differentiate the rate of CO methanation on a Pd/SiO2 catalyst; (3) development of an extended x-ray absorption spectroscopy technique to determine the number of surface Pd atoms with a particular coordination number utilizing inert gas adsorption; and (4) synthesis and characterization of bimetallated TiO2 nanorods for future studies as catalysts for total water splitting. The development of time-resolved infrared spectroscopy is still in its infancy for the study of chemical kinetics and dynamics in heterogeneous catalysis. Preliminary results with photolytic ethylene generation has provided promising results towards the identification of reaction intermediates during hydrogenation, and we continue to pursue these approaches for selective oxidation of olefins.

15. SUBJECT TERMS

heterogeneous catalysis, kinetics, dynamics, catalytic cycles, infrared spectroscopy, time resolution, x-ray absorption spectrosco

16. SECURITY CLASSIFICATION OF:			**17. LIMITATION OF ABSTRACT**	**18. NUMBER OF PAGES**	**19a. NAME OF RESPONSIBLE PERSON**
a. REPORT	**b. ABSTRACT**	**c. THIS PAGE**			**19b. TELEPHONE NUMBER** *(include area code)*

Air Force Office of Scientific Research Final Report

Final Report for "*Dynamic Chemical and Structural Changes of Heterogeneous Catalysts Observed in Real Time: From Catalysis-Induced Fluxionality to Catalytic Cycles*" (FA9550-12-1-0204)

Robert M. Rioux
Department of Chemical Engineering
Department of Chemistry
The Pennsylvania State University
University Park, PA 16802-4400 USA

Summary of final report

The results from "Dynamic Chemical and Structural Changes of Heterogeneous Catalysts Observed in Real Time: From Catalysis-Induced Fluxionality to Catalytic Cycles" are summarized in this final report. The period of the grant was reduced from 3 years funding to two years funding with a six-month no cost extension. Therefore, the results included in this work were collected from 4/15/2012 to 10/14/2014. The project continues in the Rioux laboratory, and many of the results that are currently being collected on the step-scan infrared spectrometer will be published and the AFOSR Molecular Dynamics grant will be acknowledged according. In this report, our efforts towards achieving our proposed research objectives will be summarized, including (1) construction and evaluation of a transmission infrared spectroscopy cell utilizing either a pulsed valve or laser pulse to generate temporal perturbation that enables millisecond to microsecond time resolution; (2) our initial results utilizing millisecond-wide pulses to titrate kink, step and terrace sites, followed by their removal with pulsed oxygen in order to differentiate the rate of CO oxidation on a real Pd/SiO_2 catalyst; (3) development of a new extended x-ray absorption spectroscopy technique to

Part I. Construction and evaluation of a transmission infrared spectroscopy cell for rapid-scan and step-scan infrared measurements

We began the project by building two different transmission infrared cell to study heterogeneous catalysts during gas-phase reactions. The first is a rectangular welded stainless-steel body that is fitted with a heating stage composed of fitted copper contacts that send current through a W mesh that resistively heats the catalyst sample. **Figure 1** is a SolidWorks drawing and photograph of the 1st generation rapid-scan capable cell. We have improved upon the heating capabilities of this cell while utilizing the same cell body. On the left-hand side is the fast-switching valve. Utilizing a home-built pulse driver, this valve can be opened and closed in 10 msec. This valve represented an excellent starting point to conduct rapid-scan infrared spectroscopy measurements on heterogeneous catalysts. We utilized (see Section

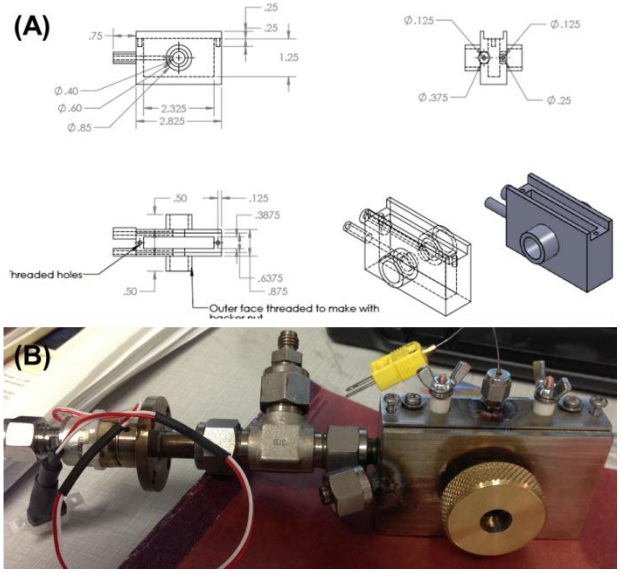

Figure 1. (A) Solidworks drawings of transient infrared cell. (B) Photograph of rapid-scan transient cell for gas-phase measurements.

II) a Bruker Vertex 80V spectrometer with rapid scan capabilities in order to examine the utility of cell. We initially examined the adsorption of NO and its displacement by carbon monoxide to quantify the time resolution. We will not present the details of the characterization of the cell since it will appear in a paper that has recently been accepted to the *Journal of the American Chemical Society*. The results of the control experiment demonstrated that a 10 ms wide pulse of gas-phase CO resides in the low-volume reactor for 5s in the case of a bed (pure silica) that does not adsorb CO. This provided the amount of time required between subsequent pulses of reactive gas. To ensure, reproducible results, we provide 10 s between pulses and utilized the scheme in **Figure 2** to collect rapid-scan data.

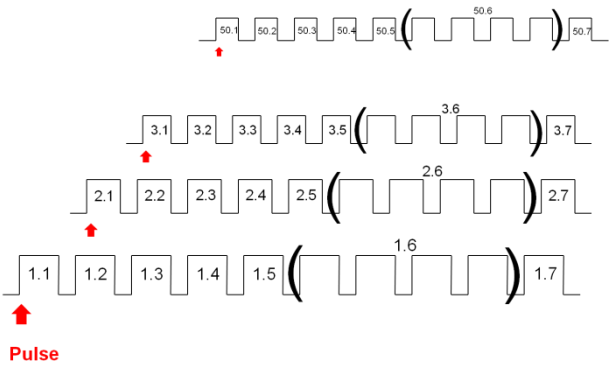

Figure 2. Principle of rapid-scan FTIR spectroscopy. The measurement must be repeated numerous times in order to obtain sufficient S/N to noise. The red arrows in the figure demonstrate the initial and subsequent pulses of reactant (either through photoexcursion of a reactant or a mechanical valve). In this schematic, 50 pulses are demonstrated.

A second cell (picture not included) was developed and tested for step-scan measurements where the transient pulse of reactant was generated by photoexcursion of small molecules. For example, Frei and co-workers have studied the diffusion of CO in silica at microsecond timescale through the photoexcursion of CO from diphenylcylcopropanone using a nanosecond UV laser. We have it difficult to reproduce these results, and believe that the problem of irreproducibility is primarily associated with sample preparation. Sample preparation relies on the impregnation of your photolabile precursor into your catalyst matrix. If this impregnation is non-uniform, it is difficult to accomplish the experimental procedure outlined in Figure 2. This inability to reproducibly disperse the photo-labile molecule through the catalyst matrix has impeded our ability to make progress utilizing diphenylcyclopropanone as a photolabile molecule to generate CO in-situ. However, for reaction involving ethylene as a reactant, we have successfully developed a procedure utilizing *n*-ethyluracil to photoextract ethylene. At this point, it is unknown why the impregnation of ethyluracil is more reproducible than diphenylcylcopropanone. We are continuing our efforts to extract transient data from step-scan measurements

Part of this work has been submitted (7/2014) and re-submitted (11/2014) to the *Journal of the American Chemical Society*. Additional manuscripts acknowledging FA9550-12-1-0204 are currently in various stages of preparation.

Part II. Demonstration of the rapid-scan capabilities of the transmission infrared spectroscopy cell for the site-selective hydrogenation of carbon monoxide: In-situ differentiation of the reactivity of kink, step and terrace sites

The conversion of carbon monoxide is critical to a number of technologies. In particular, the catalytic conversion of synthesis gas (CO/H_2) is vital since it the primary route to methanol and synthetic fuels via the Fischer-Tropsch process. One reaction that is particularly detrimental to the Fischer-Tropsch process is the methanation of carbon monoxide to methane ($CO + 3H_2 \rightarrow CH_4 + H_2O$) since it produces a gaseous product (CH_4) with little value and consumes significant amounts of an expensive fuel (H_2). Therefore, we examined the methanation of CO/H_2 mixtures utilizing rapid-scan infrared spectroscopy over Pd, Co

and Fe catalysts. Although, Fe and Co are relevant metals in FT catalyst formulations, we have included Pd catalysts because Pd or Pt is commonly included in FT catalyst formulations at very low levels to aid in the reduction of Co or Fe since it is a potent catalyst for H_2 activation. Therefore, even at low levels, Pd may play a primary role in the formation of CH_4 since it activates H_2 and does not have a propensity to form C-C bonds. **Figure 3** is an example of the growth of adsorbed CO on a Pd/SiO_2 catalyst after a number of pulses of 1% CO. As one can see that the intensity of the CO grows linearly with time (proportional to the number of CO pulses). The ordinate in Figure 3 represents the adsorption of CO in all adsorbate configurations on Pd. However, individual rapid scan spectra demonstrate that the integrated peak in Figure 3 is representative of CO bound in a numerous configuration on Pd.

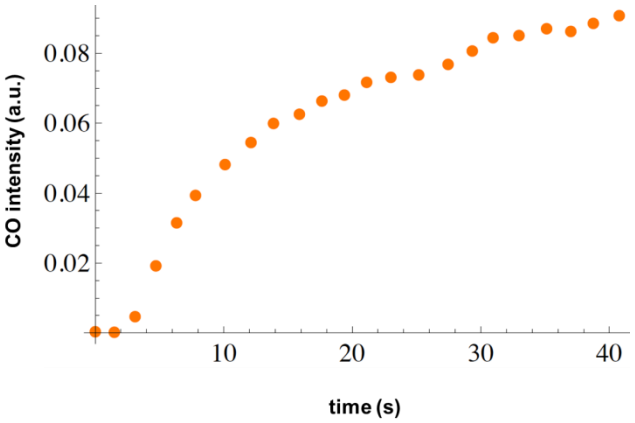

Figure 3. Intensity of adsorbed CO with time on a 1% Pd/SiO_2 catalyst reduced at 400°C in the rapid-scan transmission infrared cell. The x-axis represents the total time of the experiment (pulse time (~30 ms) + time to sweep out gaseous CO (2 s)). Only 2 seconds was required for sweeping out the gas-phase CO because >99% adsorbed at these low coverage limits.

Figure 4 shows the compiled steady-state transmission spectra of adsorbed CO on the 1% Pd/SiO_2 catalysts with differing particle size. For the catalyst with the smallest Pd particle size, there is a large absorbance around 2090 cm^{-1} which is attributed to linear bound CO, and another peak at ~1950 cm^{-1} which is assigned to bridge-bonded CO. As the particle size increases there is a sharp decrease in the linearly adsorbed CO (~2090 cm^{-1}). The absorbance of the bridge-bonded CO peak (~1950 cm^{-1}) decreases with particle size but the overall linear-to-bridging ratio still decreases with increasing particle size (Table 4). At larger Pd sizes (> 1 nm), the bridge-bonded CO peak at ~1950 cm^{-1} splits into two distinct peaks. These two peaks can be attributed to bridge-bonded CO on terraces and bridge-bonded CO on corner and edge sites. These results are consistent with an increasing ratio of large, flat surfaces (represented by bridge-bonded CO) as particle size increases. These results are consistent with those by Bradley et al. This data demonstrates that a variety of CO-Pd species form and their populations can be controlled by the equilibrium pressure of CO.

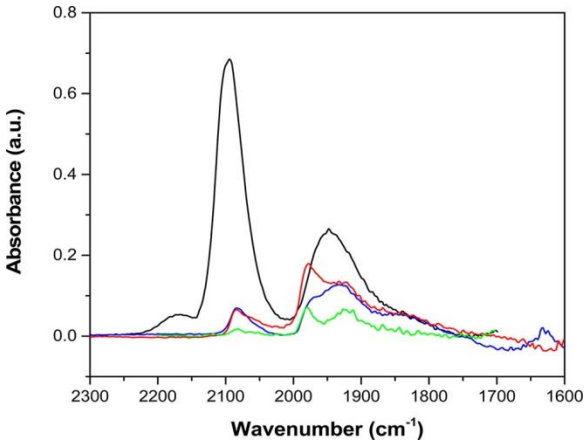

Figure 4. DRIFTS spectra of the adsorption of carbon monoxide on silica-supported Pd catalysts at room temperature. 1.0 nm (black line), 2.5 nm (blue line), 3.0 nm (red line) and 8.1 nm (green line)

We have utilized the ability to identify the adsorption site of CO on Pd catalysts to understand their intrinsic reactivity under 10 ms pulses of hydrogen. Under limiting conditions of H_2 per pulse, we effectively titrate CO adsorbed to certain sites on the catalyst. These experiments conducted by rapid-scan infrared spectroscopy does not allow to calculate absolute rates because it is difficult to measure the extinction coefficient associated with each CO-Pd

species, but it allows us to calculate the relative rates of CO methanation on each site type (kink, step, terrace). The relative rates (setting the rate of methanation on the terraces to 1) are kinks (10^2): steps (40) and terraces (1). We believe this is the first *in-situ*, direct quantification of the reactivity of individual sites on the same catalyst. We are currently developing microkinetic models based on

This work has been submitted in two separate manuscripts to the *Journal of Catalysis* (October 2014) and *ACS Catalysis* (November 2014). Additional manuscripts acknowledging FA9550-12-1-0204 are currently in various stages of preparation.

Part III. Illuminating Surface Atoms in Nanoclusters by Differential X-ray Absorption Spectroscopy

We use differential extended x-ray absorption fine structure (Δ-EXAFS) to monitor the Ar-induced surface restructuring of silica-supported Pd nanoclusters (1 nm diameter) at 77 K. Δ-EXAFS analysis shows 9 ± 2 nearest-neighbor Pd-Pd bonds expand by 0.104 ± 0.005 Å as a result of Ar adsorption. Atomistic molecular dynamics simulations provide evidence for a model in which Ar drives restructuring of under-coordinated Pd atoms, leading to an increased Pd-Pd bond length of surface Pd atoms with no change in overall nearest-neighbor Pd-Pd coordination number. Based on observations from the atomistic simulations, it is likely that under-coordinated atoms are trapped in metastable states at 77 K and Ar provides the kinetic energy needed to overcome the barrier for surface restructuring. Together, experiment and theory highlight the ability of Δ-EXAFS to probe surface atoms of Pd nanoclusters.

Despite the number of methods developed in the last decade, improving the selectivity of structural probes to surface metal atoms in nm-scale nanoclusters remains one of the primary objectives of catalysis science. In this work we will show the application of a Δ-EXAFS method that we developed for probing surface atoms of SiO_2-suppoted Pd nanoclusters. The Δ-EXAFS data were obtained by measuring the EXAFS signals before and after Ar adsorption, and subsequently modeled by taking into account only the unsubtracted, surface Pd contributions. In addition to EXAFS data analysis and modeling, we have also employed atomistic molecular dynamics (MD) simulations to differentiate between models compared in the EXAFS data analysis process, thus determining the most plausible mechanism for restructuring. Further application of the technique is not limited to a particular set of materials; instead, it can be applied to any system in which modulation causes small changes in local structure.

Experimental and Computational Methods

Synthesis of Pd/SiO_2

A 3% Pd/SiO_2 was synthesized using the strong electrostatic adsorption (SEA) method, according to a previously reported procedure. $Pd(NH_3)_4(NO_3)_2$ was added to a slurry of silica (Davisil A60) at pH = 11. The sample was filtered, washed, and dried at 398 K prior to reduction at 438 K under flowing 4% H_2/He for 1 h.

X-ray Absorption Spectroscopy (XAS)

XAS measurements were performed at beamline 10-BM of the Advanced Photon Source (APS) at Argonne National Lab (ANL). The 3% Pd/SiO_2 catalyst (~50 mg) was pressed into a 4 mm ID cylindrical steel holder to obtain an edge step of ~0.4 at the Pd K-edge. The sample was loaded into a specially designed *in situ* reactor cell capable of heating the catalyst sample to 523 K for reduction and cooling to 77 K during XAS measurements. After loading the sample, the sample chamber was evacuated with a mechanical vacuum pump to a base pressure of 30 mTorr subsequently pressure checked to ensure

all fittings were installed correctly and the system had no leaks. Ultra-high purity (UHP, 99.999%) 3% H_2/He without further purification was used for reduction of the catalyst. All UHP grade gases were purchased from Praxair/GTS Welco. The concentration of the analyzed impurities in UHP He were O_2 (< 1 ppm), H_2O (< 0.5 ppm) and total hydrocarbons (THC, < 0.5 ppm) and N_2 (< 5 ppm). The UHP Ar contained O_2 (< 1 ppm), H_2O (< 3 ppm) and total hydrocarbons (THC, < 0.5 ppm) and N_2 (< 4 ppm). UHP He and UHP Ar were passed through triple gas purifiers (Restek Super Clean gas purifier) to remove oxygen, moisture, and hydrocarbons to a purity of 99.9999% prior to admission onto the catalyst sample. The sample was purged at room temperature under flowing 3% H_2/He at a rate of 30 mL/min for 15 min before heating to 523 K and holding for 1 h. The system was purged with He at a rate of 30 mL/min for 20 min prior to cooling to remove absorbed and adsorbed hydrogen from the Pd nanoclusters (NCs). The sample was then immediately cooled to 77 K by sliding the sample holder into the liquid nitrogen Dewar with a magnet. The temperature of the catalyst was measured in a separate experiment to be 79 K. However, it is unclear if the thermocouple was inducing a heat loss and was the cause of the increased temperature. Therefore, the temperature of the EXAFS measurements is assumed to be 77 K. All EXAFS scans were acquired in transmission geometry with an energy range from 200 eV before to 1227 eV after the Pd K-edge (24350 eV). A reference Pd foil was placed between the transmission and reference ionization chambers for energy calibration and alignment. The EXAFS scans referred to as "Clean Pd NCs" were acquired under flowing He at a rate of 30 mL/min at 77 K. The EXAFS scans referred to as "After Ar adsorption" were acquired under a mixture of Ar (5 mL/min) and He (30 mL/min) at 77 K. At this partial pressure of Ar (~100 Torr), we expect both the silica and Pd surface to be covered by approximately one statistical monolayer of Ar based on BET surface area measurements. The IFEFFIT package was used for XAS data processing, and analysis. Energy calibration was performed by aligning all scans with the reference Pd foil prior to further processing. Energy calibration was performed by aligning all scans with the reference Pd foil prior to further processing. In addition, the parameters used for background normalization were kept constant for all scans to ensure that no artifacts were generated from the data normalization procedure. To ensure the differential EXAFS oscillation produced as a result of subtracting the EXAFS scans before and after Ar adsorption is not due to a slight shift in the zero-point calibration of the k-scale, we also reproduced the differential spectrum without alignment of each scan with the reference Pd foil. Additionally, the data normalization procedure is reproducible across multiple EXAFS scans.

Scanning Transmission Electron Microscopy (STEM)

STEM images were acquired at the University of Chicago Research Resources Center facility using a JEOL-ARM 200CF aberration corrected microscope (70 pm spatial resolution and 300 meV energy resolution). STEM imaging for this sample was previously reported. Samples were prepared for analysis by dispersing in isopropyl alcohol, sonicating for 20 min, dropping onto a holey-carbon copper grid, and drying under a heat lamp for 20 min. Images were taken using the High Angle Annular Dark Field (HAADF) mode and the Particle2 program was used for counting particle sizes. 90 particles were counted to get a representation of the particle size distribution.

Computational Method

ReaxFF is a classical interatomic interaction force-field that consists of both bonding and non-bonding interactions, which enables the potential to describe both metallic bonding and van der Waal interactions that occur in a system consisting of Pd clusters exposed to a noble gas. To conduct simulations involving metal/metal and metal/noble gas interactions, we combined a recently developed

ReaxFF Pd/Pd interaction potential (which was trained against DFT and experimental structural data and formation energies for Pd bulk, surfaces, and clusters) with Ar and He parameter sets. Model Pd_{43} clusters (1 nm diameter) were generated using a hybrid Monte Carlo-molecular dynamics scheme (MC/MD), in which MC steps randomly displace Pd atoms in the cluster according to the usual Metropolis criteria. After every 500 MC trial steps, a 100 ps MD run was conducted to diversify the configuration space explored by the cluster. The temperature of the MC/MD simulation was set to 500 K, which corresponds to the temperature of the experimental system prior to being quenched to 77 K. Hence, the MC/MD simulation yields a set of model clusters in reasonable approximation to those contained in the poly-disperse experimental sample upon exposure to Ar gas, albeit not including the silica support present in the experimental system.

To assess the impact of an Ar gas phase on Pd cluster reconstruction, we conducted molecular dynamics simulations in the NVT ensemble *via* the velocity Verlet method with a 0.25 fs time step. A Berendsen thermostat[27] with a damping constant of 100 fs was used to maintain a temperature of 77 K through the duration of the 1 ns simulations. The model clusters were equilibrated for 1 ns in vacuum before being exposed to 50 gas phase Ar atoms in a 50×50×50 Å periodic simulation cell (yielding an effective pressure of ~0.5 MPa, estimated from the ideal gas law) for an additional 1 ns. Average Pd-Pd bond distances were determined for each atom from atomic coordinates that were archived at 125 fs intervals throughout the simulation. Additional control simulations were conducted under He to ensure that observed Pd cluster reconstructions can be attributed to the Ar gas phase.

Nearest-neighbor (NN) coordination numbers were calculated using a cutoff radius of 3.5 Å around each atom. The Ar-induced bond length expansion was calculated by taking the difference between the average NN bond length of each atom before and after being exposed to Ar. The data were averaged over the last 125 ps (1000 frames) of each simulation to obtain representative NN bond lengths and coordination numbers.

Results

Adsorption of Ar on Pd/SiO_2 at 77 K

The Pd K-edge EXAFS data for the Pd NCs at 77 K under a He atmosphere (30 mL/min) are shown in **Figure 5** (referred to as "Clean Pd NCs"). After reduction at 523 K with 3% H_2/He, the sample was purged with pure He prior to cooling to prevent palladium hydride (PdH_x) formation. Based on the Pd-Pd first shell bonding distance, it is clear PdH_x is absent in the sample. The data show only Pd-Pd bonding and there is no indication of low-Z scatterers (e.g. C, O, or N). The first shell was modeled with a single Pd-Pd scattering path and the fit is shown along with the data in Figure 5. The results of the fit are shown in Table 1. The clean Pd NCs have a Pd-Pd coordination number and bond length of 7.0 ± 0.2 and 2.700 ± 0.005 Å, respectively. The bond length is contracted with respect to Pd foil, indicating the presence of small Pd NCs, which is in agreement with STEM data. The coordination number is consistent with Pd nanoclusters of about 37 atoms (Pt_{37}). A Pd_{37} cluster with the hemispherical (111)-truncated cuboctahedron geometry has a fist shell coordination number of 6.97 and diameter of 1.1 nm. Attempts to fit the EXAFS data past the first coordination shell following established methods failed due to the high disorder of the ultra-small Pd NCs. A STEM image for the sample is shown in **Figure 6**. The average particle size determined from STEM is 1.0 ± 0.2 nm, which is consistent with the EXAFS results (1.1 nm).

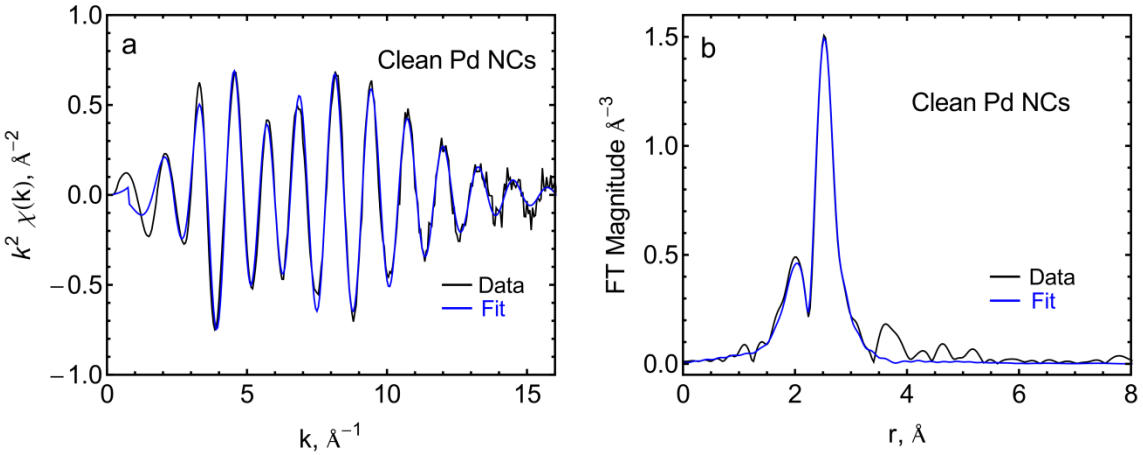

Figure 5 (a) Edge-step normalized and background-subtracted k^2-weighted $\chi(k)$ EXAFS data and (b) Fourier transform magnitude of k^2-weighted $\chi(k)$ for the clean Pd NCs in He atmosphere at 77 K at the Pd K-edge. The first-shell fit of the data is shown in blue.

Table 1 Pd K-edge EXAFS first shell fits.

Sample	**N**[a]	**r (Å)**	**σ^2** [b] **(Å^2)**
Pd Foil	12	2.731 ± 0.002	0.0058 ± 0.0002
Clean Pd NCs	7.0 ± 0.2	2.700 ± 0.005	0.0088 ± 0.0002
After Ar Adsorption	7.2 ± 0.4	2.707 ± 0.008	0.0094 ± 0.0004

[a]Calculation of N was performed using the amplitude reduction factor obtained from the Pd foil (0.86).
[b]EXAFS Debye-Waller factor.

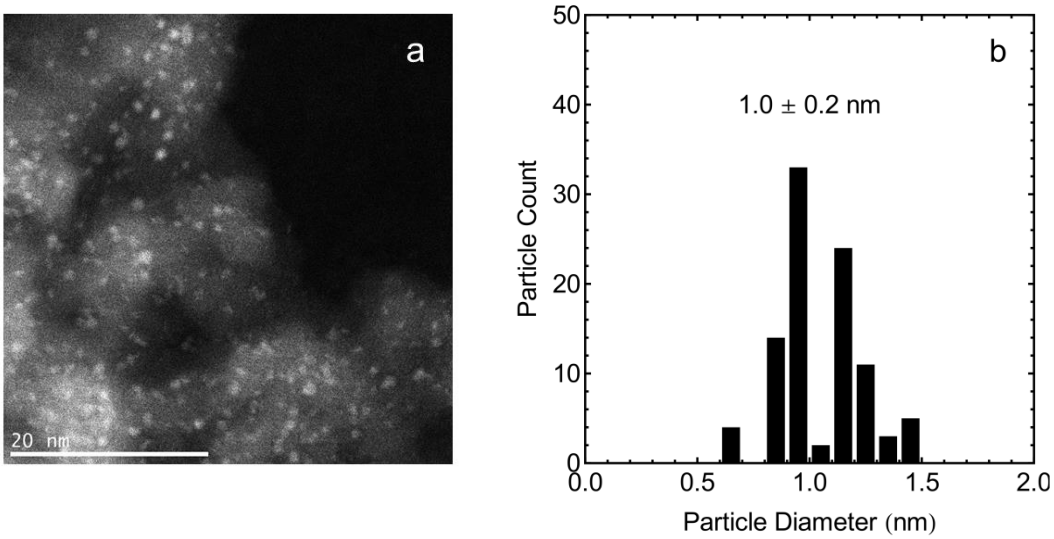

Figure 6 (a) STEM image of Pd/SiO_2 nanoclusters and (b) particle size distribution of Pd/SiO_2 catalyst. The calculated number average particle diameter is 1.0 ± 0.2 nm.

After Ar adsorption (5 mL/min Ar in 30 mL/min He), the EXAFS data highly resemble the data for the clean Pd NCs. The first shell fit of the data after Ar adsorption provides identical results (within error) to the clean Pd NCs. This analysis strategy, however, is not adequate for detection of changes that may have occurred in Ar atmosphere because only a few surface atoms of Pd particles would have been affected by Ar while XAS signal probes all atoms in the NC. Differential EXAFS (Δ-EXAFS) spectrum

obtained after subtracting the two spectra (the one measured in Ar from the other, measured in He) should have much greater sensitivity to the atoms directly affected by Ar because the contributions to the Δ-EXAFS from unaffected ("spectator") atoms will cancel. The Δ-EXAFS signal is shown in **Figure 7**. The most striking characteristic of this spectrum is a shift of the phase of the oscillations by ca. π/2, clearly visible in Figure 7. We will show analytically below that the π/2 phase shift in the Δ-EXAFS compared to the total spectrum is consistent with a small change of the Pd-Pd bond length provided that the total coordination number of Pd atoms remains approximately the same. After the adsorption of Ar, the sample was heated to room temperature and purged with flowing He (30 mL/min) and subsequently cooled to 77 K. Taking the difference of the clean Pd NCs EXAFS spectrum and a spectrum after heating to room temperature shows only noise; therefore, the observed change in the Pd bond length is reversible.

We believe that the Δ-EXAFS signal arises soley due to Ar adsorption, and is not influenced by any impurities present in the inert gas streams. Based on the amount of oxygen, nitrogen and water present in either the He or Ar cylinder, the number of surface Pd atoms present in the Pd/SiO_2 catalyst is ~10^4 greater than the number of impurity molecules introduced to the catalyst over the course of the entire experiment. Additionally, the UHP He contains similar impurities to that of UHP Ar, so if O_2 or H_2O were the primary cause of the observed results we would expect it to do so similarly both before and after the introduction of Ar and cancel after taking the differential spectrum. The XANES of the Pd NCs show little difference before and after Ar adsorption, indicative of no change in electronic structure of the Pd atoms.

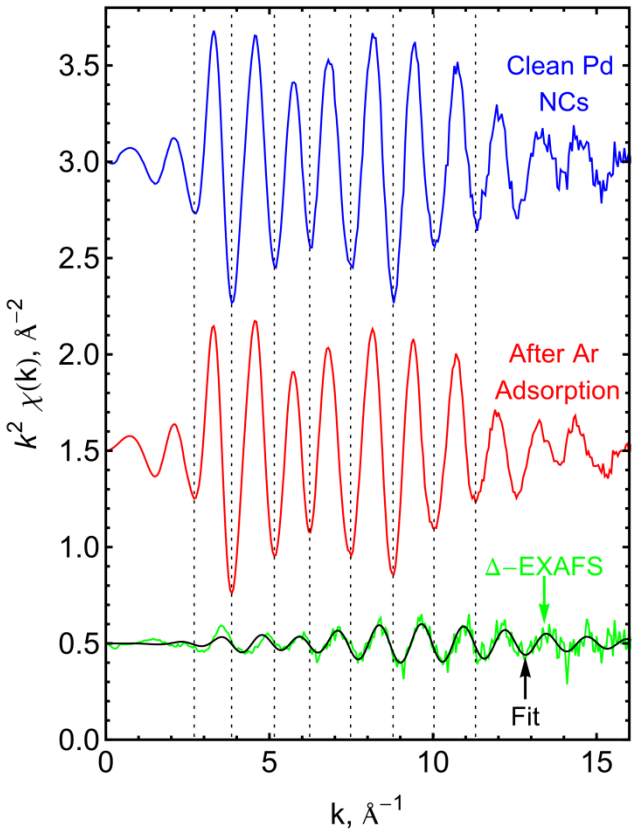

Figure 7. k^2-weighted $\chi(k)$ EXAFS data for the clean Pd NCs, after Ar adsorption, and the Δ-EXAFS spectrum obtained by subtracting the spectrum after Ar adsorption from the clean Pd NCs spectrum. The fit of the Δ-EXAFS data is shown in black. The dotted lines are a guide to the eye to show the π/2 phase

shift of the Δ-EXAFS compared to the original spectrum for Pd NCs. The data are shifted vertically for clarity.

Below, we describe a general method useful for the analysis of differential EXAFS data of small metal nanoclusters and provide a quantitative assessment of the restructuring of the Pd NCs. The EXAFS signal $\chi(k)$ for modeling the first shell scattering of a NC, with two types of bonds, core (*i*) and surface (*i*') (prime refers to surface bonds), is shown below:

$$\chi(k) = \frac{S_0^2 N_i f(k) e^{-\frac{2r_i}{\lambda(k)}} e^{-2k^2\sigma_i^2}}{kr_i{}^2} \sin\big(2kr_i + \delta(k)\big) + \frac{S_0^2 N_{i'} f(k) e^{-\frac{2r_{i'}}{\lambda(k)}} e^{-2k^2\sigma_{i'}^2}}{kr_{i'}{}^2} \sin\Big(2kr_{i'} + \delta(k)\Big) \quad (1)$$

where *k* is the photoelectron wave number, S_0^2 is the passive electron reduction factor, $f(k)$ and $\delta(k)$ are the photoelectron scattering-path amplitude and phase, respectively, N is the coordination number, *r* is the interatomic distance, σ^2 is the mean-square deviation in *r*, and $\lambda(k)$ is the photoelectron mean free path. Correspondingly, the EXAFS equation for the "Clean Pd NCs" sample, χ_{Clean}, is:

$$\chi_{Clean}(k) = \frac{S_0^2 N_1 f(k) e^{-\frac{2r_1}{\lambda(k)}} e^{-2k^2\sigma_1^2}}{kr_1{}^2} \sin\big(2kr_1 + \delta(k)\big) + \frac{S_0^2 N_{1'} f(k) e^{-\frac{2r_{1'}}{\lambda(k)}} e^{-2k^2\sigma_{1'}^2}}{kr_{1'}{}^2} \sin\Big(2kr_{1'} + \delta(k)\Big) \quad (2)$$

The EXAFS equation for the "After Ar adsorption" sample, χ_{After}, is:

$$\chi_{After}(k) = \frac{S_0^2 N_2 f(k) e^{-\frac{2r_2}{\lambda(k)}} e^{-2k^2\sigma_2^2}}{kr_2{}^2} \sin\big(2kr_2 + \delta(k)\big) + \frac{S_0^2 N_{2'} f(k) e^{-\frac{2r_{2'}}{\lambda(k)}} e^{-2k^2\sigma_{2'}^2}}{kr_{2'}{}^2} \sin\Big(2kr_{2'} + \delta(k)\Big) \quad (3)$$

Since the interior atoms are unchanged during the adsorption of Ar, $N_1 = N_2$, $r_1 = r_2$, and $\sigma_1^2 = \sigma_2^2$. In addition, S_0^2, $f(k)$, and $\lambda(k)$ will be identical in all terms since they all refer to a Pd-Pd single scattering path. The number of surface atoms, $N_{1'}$ or $N_{2'}$ will also remain unchanged and this will be referred to as N_s. If Eq. (3) is subtracted from Eq. (2), the following expression is derived for Δ-EXAFS ($\chi_{Clean} - \chi_{After}$):

$$\Delta\text{-EXAFS} = \frac{S_0^2 N_s f(k) e^{-\frac{2r_{1'}}{\lambda(k)}} e^{-2k^2\sigma_{1'}^2}}{kr_{1'}{}^2} \sin\Big(2kr_{1'} + \delta(k)\Big) - \frac{S_0^2 N_s f(k) e^{-\frac{2(r_{1'}+\Delta r)}{\lambda(k)}} e^{-2k^2\sigma_{2'}^2}}{k(r_{1'}+\Delta r)^2} \sin\Big(2k(r_{1'} + \Delta r) + \delta(k)\Big) \quad (4)$$

where $r_{2'}$ is expressed as $r_{1'} + \Delta r$. We note that Eq. (4), in the approximation that the bond length disorder did not change between the two states, and that $\Delta r \ll r$, reduces to a simple ansatz (a complete derivation of Eq. 5 is provided in the ESI):

$$\Delta\text{-EXAFS} \approx \frac{S_0^2 N_s f(k) e^{-\frac{2r_{1'}}{\lambda(k)}} e^{-2k^2\sigma_{1'}^2}}{kr_{1'}{}^2} (2k\Delta r) \sin\Big(2kr_{1'} + \delta(k) + \frac{\pi}{2}\Big) \quad (5)$$

Eq. (5) shows that for small variations in the bond length, Δr, the differential EXAFS spectrum will display a π/2 phase shift compared to the original EXAFS spectrum (χ_{Clean}). This validates our conclusions based on visual examination of the Δ-EXAFS (Figure 7) which also shows the π/2 phase shift compared to the spectrum measured in He or Ar atmospheres. We note that Eq. (5) is equivalent to that used for analysis of differential signal in magnetostriction experiment by modulation excitation method.

The differential spectrum can be modeled by implementing Eq. (4) into a suitable data analysis program. In this work it was accomplished by using FEFF models for each spectrum and fitting the difference between the two modeled signals to the experimental data. The total number of Pd-Pd bonds affected by Ar adsorption, $n_{Pd-Pd,aff}$, can be estimated directly from the measured N_s, the coordination number of Pd-Pd atoms in the differential spectrum, and the total number of atoms in a representative particle (n) as follows:

$$N_s = \frac{2n_{Pd-Pd,aff}}{n} \quad (6)$$

We note that the denominator is the total number of atoms per particle, not the total number of affected atoms, which would make it analogous to a conventional expression for coordination number[31] because the differential signal was obtained by subtracting the edge-step normalized EXAFS spectrum. Edge step normalization is the procedure that relates the total EXAFS signal from all absorbing atoms in the sample to that corresponding to an "an equivalent absorber", hence, the total number of atoms is used in the denominator of Eq. (6).

The terms $r_{1'}$ and $\sigma^2_{1'}$ were obtained from the fit of the "Clean Pd NCs" (Figure 5 and **Table 1**) under the approximation the surface atoms have a bond length and EXAFS Debye-Waller factor equivalent to the bulk value of the Pd NCs (i.e. $r_1 = r_{1'}$ and $\sigma^2_1 = \sigma^2_{1'}$). However, in other cases, higher data quality may allow for the determination of $r_{1'}$ and $\sigma^2_{1'}$ directly from the differential data.

The results of fitting the Δ-EXAFS with Eq. 4 are presented in **Table 2** and the Fourier transform magnitude EXAFS for the data and the fit are presented in **Figure 8**. The number of Pd-Pd bonds that changed during the Ar-induced restructuring is 9 ± 2. These bonds expanded by Δr = 0.104 ± 0.005 Å. In addition, the disorder of these bonds decreased since the EXAFS Debye-Waller factor decreased from 0.0088 ± 0.0002 to 0.0045 ± 0.0009. Thus, the EXAFS analysis shows that 9 ± 2 NN Pd-Pd bonds expand as a result of introducing Ar at 77 K. This is compared to the total number of NN Pd-Pd bonds in a 37-atom Pd cluster of 129.

Table 2 Fit parameters obtained from the differential data using Eq. (4).

Parameter	Value	Allowed to Vary?
N_s	0.46 ± 0.07	Yes
$r_{1'}$	2.700 ± 0.005 Å	No[a]
$\sigma^2_{1'}$	0.0088 ± 0.0002	No[a]
Δr	0.104 ± 0.005 Å	Yes
$\sigma^2_{2'}$	0.0045 ± 0.0009	Yes
$n_{Pd-Pd,aff}$	9 ± 2	[b]

[a]Obtianed from fit of Clean Pd NCs.
[b]Determined after the fit using Eq. (6), where n = 37.

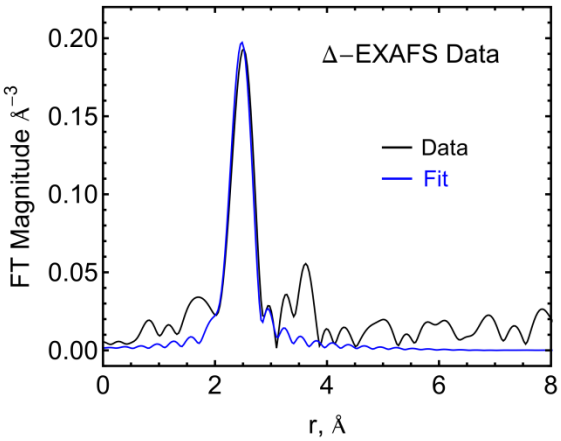

Figure 8 Fourier transform magnitude of k^2-weighted $\chi(k)$ for the Δ-EXAFS spectrum (black) and the fit of the data (blue) using the model in Eq. (4).

EXAFS analysis by fitting method often depends on the model used, and comparing several models is necessary to avoid possible misinterpretation of the data. We have compared two additional models that are described below. The first model was a Pd-Ar single-scattering model that assumes that the differential signal could arise from Pd-Ar scattering only. Attempts to fit the Δ-EXAFS signal with the Pd-Ar scattering model results in an unrealistic fit parameter for the energy shift and a poor-quality fit to the data. Therefore, we dismiss the possibility that the differential signal arises from Pd-Ar contributions. The second model was a direct fit of the differential data with Pd-Pd scattering. This model would only be appropriate if the number of Pd-Pd bonds changed, such that the amplitude of the differential data represents additional Pd-Pd bonds that arose during the adsorption of Ar (or Pd-Pd bonds that were removed during the adsorption). Fitting the differential data with this model results in a good fit to the data, and the Pd-Pd bond length expansion was comparable to what was found in the present differential model EXAFS model. However, this model assumes the overall Pd-Pd coordination number changed during Ar adsorption. On the other hand, the differential EXAFS model described in Eq. (4) shows that the differential EXAFS signal arises from a change in bond length only, with no change in the overall Pd-Pd coordination number. Thus, using EXAFS alone, it is impossible to differentiate between the two aforementioned models. We show through the atomistic modeling described below that we are able to use theory to break the degeneracy of the two competing EXAFS models.

Atomistic modeling of Ar-induced restructuring

To support our experimental observation of Ar-induced surface restructuring of Pd atoms and to differentiate between the proposed EXAFS models, we conducted a series of ReaxFF-MD simulations in which model Pd clusters were exposed to both vacuum and an Ar gas phase (i.e. 50 Ar atoms in the periodic cell) at 77 K. In each simulation, the average Pd-Pd bond distance was assessed from the atomic coordinates of the system, thus allowing changes in average Pd-Pd bond distance after the introduction of Ar atoms to be determined. **Figure 9** depicts the initial and final system geometries in an MD simulation where a 1 nm Pd cluster was exposed to Ar. As seen in the figure, Ar interacts weakly with the cluster, forming a physisorbed layer of Ar atoms on the surface of the cluster. The calculated adsorption energy for an isolated Ar atom on Pd is 1-2 kcal mol^{-1}, which is dependent on the adsorption configuration.

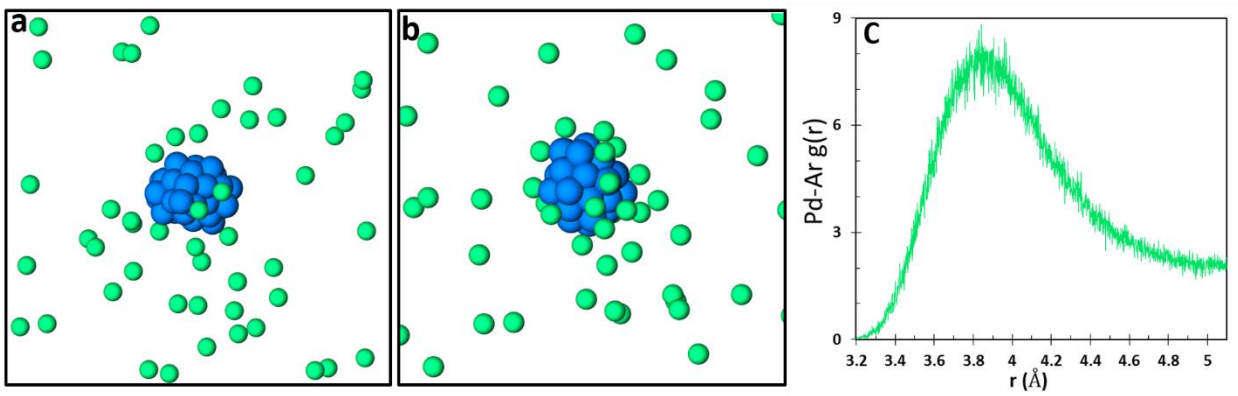

Figure 9. (a) Initial and (b) final system geometry in a 1 ns MD-NVT simulation at 77 K. (c) Pd-Ar radial pair distribution function, *g(r)*, demonstrating an Ar physisorption well centered near r = ~3.9 Å from the cluster surface.

To assure modeling results were not biased by the initial selection of cluster geometry, we employed a hybrid MC/MD simulation method to generate a set of model Pd clusters. The MC/MD simulation was conducted at 500 K, which corresponds to the experimental annealing temperature the Pd clusters were exposed to before being quenched to 77 K. This results in an ensemble of cluster geometries that are representative of those present in the experimental sample, where the energy differences between clusters arise due to thermal fluctuations in the system, as shown in **Figure 10**. The model clusters do not include the SiO_2 support used experimentally, and therefore we neglect any effect the support could have on initial Pd nanocluster structure or the restructuring process. The relative impact of this simplification is further addressed in the discussion section.

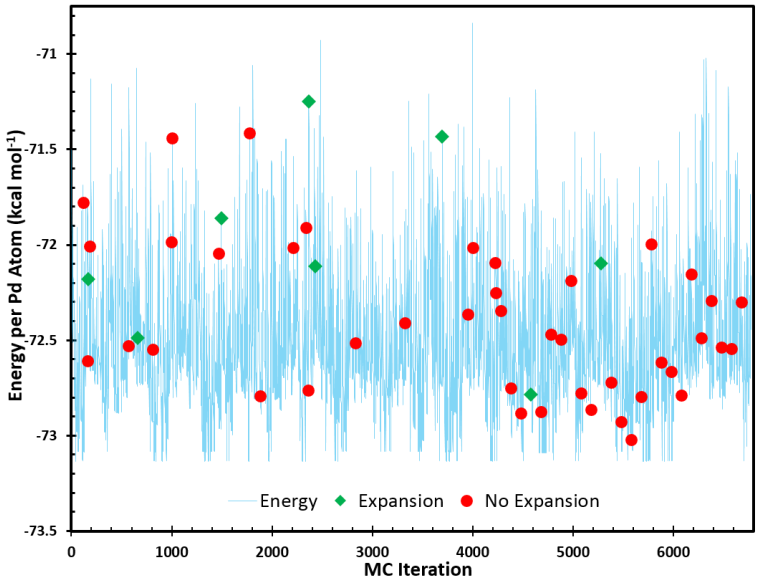

Figure 10 Energy of Pd clusters generated from a hybrid MC/MD simulation at 500 K. The green and red data points indicate clusters that were selected for separate MD simulations to assess Pd-Pd expansion upon exposure to Ar. The color coding of these dots classifies the results obtained from the subsequent 77 K MD runs in the presence of Ar. Green diamonds indicate that an average Pd-Pd expansion > 0.001 Å was observed and red dots indicate that there was no change > 0.001 Å.

We selected 50 clusters (using a random number generator) from the 500 K MC/MD sample set to serve as starting geometries for MD simulations at 77 K. The selected clusters correspond to the green and red data points in **Figure 10**. During each 77 K MD simulation, average Pd-Pd bond distances were determined by calculating the Pd-Pd radial pair distribution, *g(r)*, over the last 250 ps of the 1 ns MD simulations. As shown in **Figure 11** for a single cluster geometry, each simulation initially allows the Pd cluster to equilibrate at 77 K for 1 ns in vacuum before exposure to Ar (or He/vacuum in the case of control simulations). As seen in the figure, the simulation yields no change in Pd-Pd bond distance after exposure to vacuum or He, whereas cluster restructuring with a 0.003 Å Pd-Pd expansion occurs under Ar. The radial distribution function in Figure 9(d), in comparison to those for control simulations in Figure 11(a-c), demonstrates a clear restructuring of the cluster, where the shoulder appearing at r = ~2.60 Å in the control simulations shifts to r = ~2.75 Å (indicated by black arrows in the figure). This suggests the average Pd-Pd bond expansion can be attributed to a large increase in a few Pd-Pd bonds involving one or two atoms, as opposed to a small increase in all Pd-Pd bonds throughout the cluster. This is further depicted in Fig. 8, which shows snapshots from the 15 ps MD-trajectory window in which the surface restructuring occurs. The restructuring occurs immediately after the Pd cluster interacts with an incoming Ar atom, suggesting that the momentum transfer from the Ar atom to the cluster induces the surface reconstruction. This reconstruction does not occur in the absence of the Ar gas phase. An animated video of this 15 ps trajectory demonstrating surface reconstruction is provided in the ESI, along with a 250 ps video of the cluster in vacuum showing no reconstruction.

A similar analysis was conducted for all 50 model clusters, where 8 clusters demonstrated an average Pd-Pd bond length expansion greater than 0.001 Å upon exposure to Ar and the remaining 42 exhibited no change greater than 0.001 Å, indicated by green diamonds and red dots, respectively, in **Figure 10**. The expansion of Pd-Pd bond lengths was further quantified by assessing the average Pd-Pd bond length change for a single Pd atom as a function of its average coordination number under vacuum conditions. This is shown in **Figure 13**, where we have plotted average bond length expansion against coordination number in vacuum averaged over all 50 clusters investigated. Figure 13(a) contains data from clusters that exhibited an expansion, while Figure 13(b) contains data from clusters that did not exhibit expansion. This analysis reveals that only under-coordinated Pd atoms with low nearest-neighbor coordination numbers (i.e., 3-5) are affected by the adsorption of Ar, with a typical bond length expansion of ca. 0.05 to 0.1 Å. Figure 13(b) demonstrates some under-coordinated atoms are not affected by the Ar gas phase, indicating that some under-coordinated atoms are more stable than others. Observed coordination numbers greater than 12 reflect that these clusters have a disordered, non-crystalline lattice structure, which is expected for platinum-group-metals in this size range.[32]

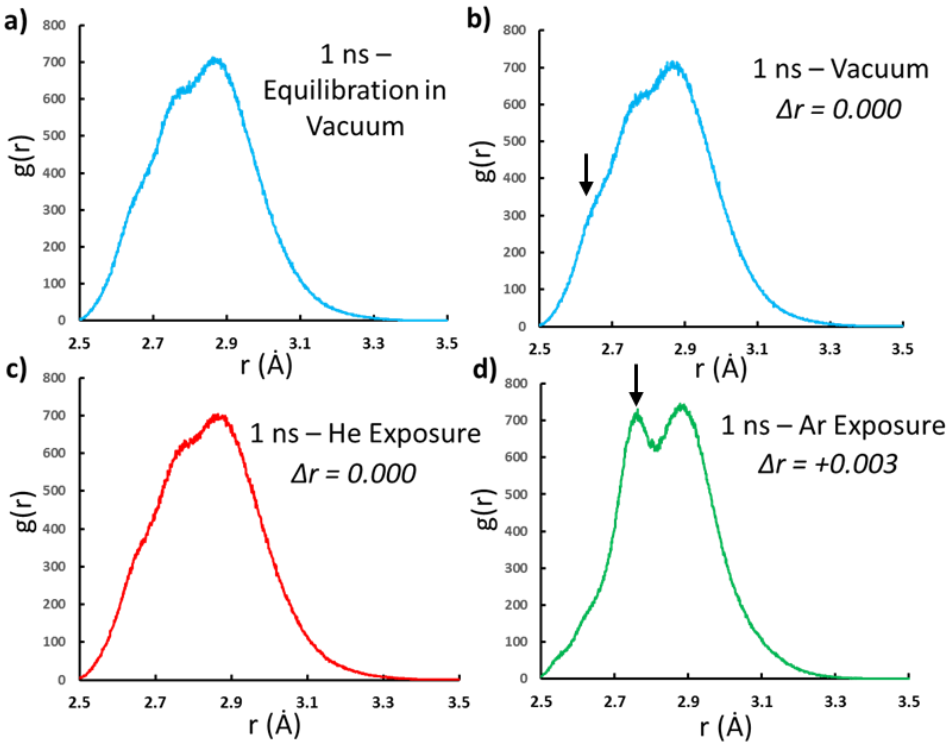

Figure 11. Pd-Pd radial distribution function, *g(r)*, reflecting the average NN Pd-Pd bond distances during a 1 ns MD simulation at 77 K. (a) The Pd cluster was first allowed to equilibrate in vacuum for 1 ns, and was then exposed to (b) vacuum, (c) He gas, or (d) Ar gas for an additional 1 ns. Arrows indicate the peak shift attributed to the average Pd-Pd bond expansion of an under-coordinated surface atom.

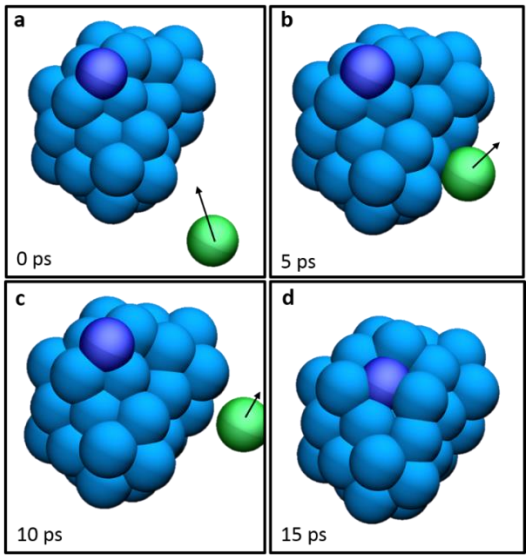

Figure 12. A 15 ps MD trajectory window demonstrating an Ar (green) collision with a Pd cluster (blue) inducing the restructuring of an under-coordinated Pd surface atom (purple). Only the Ar atom interacting with the Pd cluster is shown, all others are omitted for clarity.

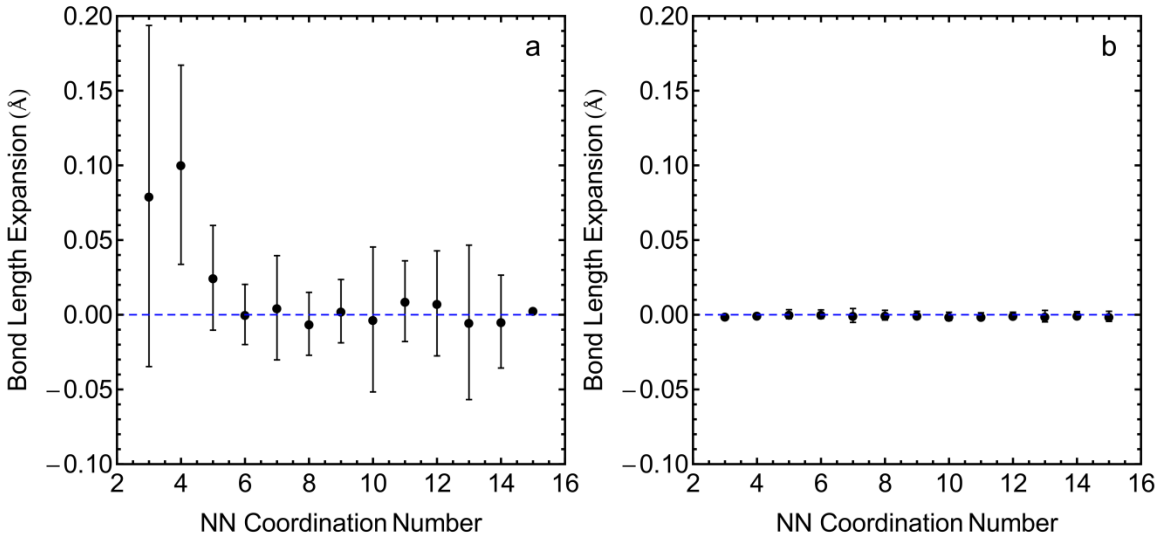

Figure 13. Bond length expansion (relative to the clusters in vacuum) plotted versus first shell coordination number for all of the atoms in each of the Pd clusters that (a) exhibited expansion and (b) did not exhibit expansion after exposure to Ar at 77 K. Error bars indicate the standard deviation in bond length of the ensemble of atoms from all of the clusters.

Since Ar induces restructuring of under-coordinated surface atoms, it is likely that these atoms are kinetically trapped in metastable positions during the quench to 77 K, and that a transfer of kinetic energy from an Ar gas phase atom provides the additional energy required to allow relaxation of the metastable Pd atom to a more favorable site with higher average coordination and longer average Pd-Pd bonds. Not all under-coordinated sites are affected by Ar, which could be the result of short simulation timescales, where a sufficient Pd-Ar interaction simply never occurred in the simulation timeframe. Also, some under-coordinated sites may be more stable than others, indicating that Ar can only induce the restructuring of sufficiently unstable Pd atoms. A ReaxFF nudged-elastic-band (NEB) barrier calculation yielded a barrier of 11.4 kcal mol^{-1} for the reconstruction shown in Figure 12, which is sufficiently high to suggest that this structure would be kinetically stable at 77 K under vacuum. Together, these simulations demonstrate Ar may drive surface reconstructions of under-coordinated atoms, thus leading to an increased Pd-Pd bond length of surface Pd atoms, in agreement with the experimental observations above.

Discussion

Analysis of the differential EXAFS data using the model in Eq. (4) shows that Ar adsorption on Pd/SiO_2 at 77 K induces small changes in the Pd-Pd coordination environment, which can be attributed to the expansion in the bond length of surface Pd atoms. However, this model was created under the presumption that the overall Pd-Pd coordination number remained unchanged during Ar adsorption, and the correctness of such an approximation can be verified by examining simulated clusters before and after Ar adsorption. We calculated the average Pd-Pd coordination number of the clusters shown in Fig. 13(a) before and after Ar adsorption. The results are presented in **Table 3**. In each of the 8 simulations in which Ar caused restructuring, under-coordinated Pd atoms formed new Pd-Pd bonds, which is concomitant with expansion in their bond length. The number of Pd-Pd bonds formed varied, as this is dependent on the starting structure. Meanwhile, a similar number of Pd-Pd bonds were broken such that the average change in Pd-Pd coordination number was ~0. Therefore, the atomistic simulations are in

agreement with the proposed differential EXAFS model in Eq. (4) and the experimental results shown in Table 2.

Table 3 Coordination environment changes of Pd clusters as a result of Ar adsorption.

Simulation[a]	# of Pd-Pd bonds formed[b]	# of Pd-Pd bonds broken[c]	Δ avg NN CN[d]
1	7.2	-9.6	-0.06
2	9.0	-9.8	-0.02
3	3.2	-1.3	0.04
4	5.1	-3.0	0.05
5	5.7	-1.0	0.11
6	4.5	-1.1	0.08
7	3.0	-5.0	-0.05
8	2.7	-7.1	-0.10
Average[e]	**5.1**	**-4.7**	**0.01**

[a]Simulations in which Ar caused restructuring.
[b]Number of Pd-Pd bonds formed during Ar adsorption.
[c]Number of Pd-Pd bonds that were broken during Ar adsorption.
[d]Average nearest-neighbor coordination number after Ar adsorption minus the average nearest-neighbor coordination number under vacuum.
[e]Average over simulations 1-8.

Restructuring without an overall coordination number change requires strongly disordered nanoclusters because restructuring of a faceted particle will always lead to either an increase or decrease in coordination number if the total number of atoms in the particle remains the same. McKenna and Shluger showed that faceted Au nanoparticles restructure under CO adsorption, leading to an increase in coordination number. Thus, for our theoretical models to be compatible with those real clusters used in our experiments, it is advantageous to model strongly disordered Pd/SiO_2 NCs rather than faceted, crystalline, structures. Experimentally it has been demonstrated that alumina- and carbon- supported Pt clusters are predominantly non-crystalline in the size range less than 1-1.5 nm.

The high effective pressure of Ar and omission of SiO_2-supported Pd NCs from the theoretical portion of this study are limitations in obtaining quantitative results of the restructuring. We expect that introduction of the SiO_2 support might result in a different distribution in Pd particle shapes and the time scale for energy transfer from Ar to Pd could be impacted by dissipation into the support. However, the overall mechanism for restructuring is likely independent of support, since the exposed Pd atoms in low coordination environments present on the Pd particle exterior, which participate in the observed restructuring, would likely not be adjacent to the support. Furthermore, the large difference in masses between Pd and SiO_2 suggest minimal vibrational coupling, and therefore we could expect that dissipation of kinetic energy passed from Ar to Pd may remain in Pd related modes on the time scale observed in the simulations. Thus, atomistic modeling qualitatively supports the hypothesis that under-coordinated surface atoms are those affected and helps us gain an atomistic level understanding of the process.

Other examples of Ar-induced restructuring include the work of Pellenq et al. who measured the neutron diffraction of ^{40}Ar adsorption in silicate-1 zeolite and showed that a step in the Ar isotherm coincides with a change in the neutron diffraction pattern. Using grand canonical Monte Carlo simulations (GCMC), the authors concluded the change in diffraction pattern can be attributed to a rearrangement of the adsorbed phase. This conclusion has been further substantiated by García-Pérez et al., who showed through GCMC simulations that a flexible host structure is likely responsible for the

stepped Ar isotherm at 77 K for a MFI zeolite. More recently, Mallon et al. surmised that the hysteresis of the Ar 87 K adsorption isotherm of silicate-1 is a result of an orthorhombic-monoclinic symmetry shift. On the other hand, Ar ion bombardment at low energy (c.a. 15 eV) has been shown to heal defects of carbon nanotubes.

We have performed steady-state experiments where only a single factor was changed at a time. Both differential spectra were measured at the same temperature (77 K). The presence of EXAFS-like oscillations of the first spectrum when Ar was present is in obvious contrast to the second spectrum that is dominated by statistical noise. In our view, this is sufficient evidence that the changes we have described are due to the influence of Ar. The second differential spectrum also characterizes temperature stability as excellent. If the sample temperature was not identical before and after Ar was replaced by He, the differential signal would have shown (and it does not) systematic features, due to the difference in the thermal factors.

The EXAFS differential data analysis method we detail is applicable to other systems where only a small fraction of surface species (active species) respond to the external stimulation (e.g. gas, pH, electric potential, temperature, etc.) while the majority of the atoms (spectators) are unaffected. In this study, we are able to measure a change in coordination environment of only 7% of the total number of Pd atoms, which highlights the sensitivity of the combined measurement and analysis scheme.

This work has been published in *Physical Chemistry Chemical Physics* (DOI: 10.1039/C4CP02146K). This manuscript acknowledges FA9550-12-1-0204 for funding. A second manuscript involving the adsorption site for Kr on silica and carbon under conditions of physical adsorption is currently under preparation.

Part IV. Quantitative Attachment of Bimetal Combinations of Transition Metal Ions to the Surface of TiO_2 Nanorods

We have examined the ability to produce bimetallic combinations of earth-abundant metals on the surface of the TiO_2 nanorods (NRs) using adsorptive decomposition methods. Our collaborators, the Hoefelmeyer group at the University of South Dakota have recently reported quantitative attachment of transition metal ions to the surface of rod-shape *anatase* TiO_2 nanocrystals, and have shown that the adsorption of metal ions to the surface of a nanocrystal is potentially competitive with selective nucleation of metal nanoparticles on the surface of nanocrystals. Complimentary to our experimental studies, we have embarked on a parallel theoretical investigation of a model system consisting of a transition metal ion on the surface of TiO_2. This work has produced predictions of electronic structure and photoexcitation dynamics of this class of materials. Namely, charge carriers formed upon band-gap excitation of the semiconductor host tend to localize on the surface transition metal ions. Such centers may participate in catalytic reactions on the surface; however the metal ions could potentially act as charge recombination centers if interfacial electron transfer reactions are slow.

Potentially, charge recombination can be prevented if separate sites for electron and hole trapping are built into the system. On this basis, we were motivated to synthesize nanocrystals with two different first-row transition metal ions on the surface. Such a bimetalated nanocrystal could assist separation of the exciton, and present distinct catalyst sites. Additionally, we note that the materials fully consist of earth-abundant materials. These materials will be subsequently studied for water oxidation utilizing step-scan infrared spectroscopy

Experimental

Chromium(III) chloride hexahydrate, iron(II) chloride tetrahydrate, copper(II) chloride dihydrate, manganese(II) chloride tetrahydrate, cobalt(II) chloride hexahydrate, nickel(II) chloride hexahydrate, oleic acid (97%, Fisher Catalog # A195-500), oleylamine (OLAM; manufactured by TCI, 50+%, Fisher Catalog # 50-014-43281), octadecene (ODE; 90%, technical grade, Fisher Catalog # AC12931-0025), isopropanol, and hexanes were used without purification. Titanium(IV)tetraisopropoxide (TTIP), 98+%, was purchased from Acros Organics.

All preparations were carried out under an atmosphere of N_2 using both Schlenk line techniques and glove box. Oleic acid stabilized rod-shape ([001] major axis) *anatase* TiO_2 nanocrystals (hereafter referred to as TiO_2 NR) were prepared according to the literature. Metallated TiO_2 NR (designated M-TiO_2 NR) were prepared according to our previously reported method.

Preparation of bimetalated TiO_2 NR (M,M'-TiO_2 NR)

Bimetalated TiO_2 NR (designated M,M'-TiO_2 NR) were prepared in all 15 combinations of any two of the following metal ions: Cr^{3+}, Mn^{2+}, Fe^{2+}, Co^{2+}, Ni^{2+}, Cu^{2+}. We note that the attachment of each metal occurs at a characteristic optimized temperature (Cr, 250°C; Mn, 200°C; Fe, 180°C; Co, 250°C; Ni, 150°C; Cu, 80°C) and OLAM:M ratio (Cr, 10; Mn, 6; Fe, 6; Co, 10; Ni, 10; Cu, 12).**Error! Bookmark not defined.** To prepare any M,M'-TiO_2 NR sample, the metals were sequentially added in a specific order in which the first metal must be one that attaches at higher temperature and the second metal at lower (or equal temperature). Thus the method for preparation of M,M'-TiO_2 nanorods is to prepare M-TiO_2 NR followed by a second metalation step at lower temperature with M' (all M-TiO_2 NR samples were isolated before use in the second metalation step). Due to similarity of the synthesis procedures for the 15 bimetal M,M'-TiO_2 NR combinations, we provide one experimental detail for preparation of Co,Fe-TiO_2 NR as an illustrative example for brevity. We note that the loading of M and M' on the surface of TiO_2 can be selected with quantitative precision and that metal loading is additive until the surface of TiO_2 becomes saturated at monolayer coverage of metals, *vide infra*.

Step 1: Synthesis of Co-TiO_2 NRs (Co:Ti = 0.05:1)

A sample of Co-TiO_2 NR was prepared according to the literature. Briefly, a 100 mL three neck flask with 1 mmol TiO_2 in hexane, 0.5 mmol oleylamine (OLAM) and 5 mL ODE was heated to 120ºC under vacuum for 30 minutes to remove the hexane and trace amount of moisture. Then, the system was cooled under N_2 to room temperature and 0.05 mmol $CoCl_2.6H_2O$ was added under N_2 atmosphere with magnetic stirring. The mixture was heated to 250°C with a heating rate of 10°C/min. The mixture was refluxed at 250ºC for 3 h with stirring after which the reaction allowed to cool to room temperature. A blue precipitate was isolated by by centrifugation at 3500 rpm for 8 minutes followed by addition of isopropanol to the blue dispersion. The precipitate was dispersible in non-polar solvents such as hexane.

Step 2: Synthesis of Co,Fe-TiO_2 NRs (Co:Fe:Ti = 0.05:0.05:1)

A 100 mL three neck flask with 1 mmol Co-TiO_2 NR (Co:Ti = 0.05:1) in hexane was evacuated to remove hexane then filled with N_2. Then 0.5 mmol oleylamine (OLAM), 5 mL ODE, and 0.05 mmol $FeCl_2.6H_2O$ were added to the Co-TiO_2 NR. The flask was fitted with a condenser under N_2 atmosphere with magnetic stirring. The mixture was heated to 180ºC with a heating rate of 10°C/min and held at this temperature for three hours while stirring. The reaction was allowed to cool to room temperature. An off green precipitate was observed upon adding isopropanol to the dispersion. After centrifugation at 3500 rpm for 8 minutes the supernatant was decanted and the precipitate could be redispersed in non-polar organic solvents.

Characterization

Powder X-ray diffraction data were acquired using a Rigaku Ultima IV powder X-ray diffractometer. The X-ray tube produced Cu Kα radiation (λ = 1.54 Å), and the generator was set to 40 kV and 44 mA during data collection. Data was collected from 20−80° (2θ). Dry TiO_2 NR powders and M,M'-TiO_2 NR powders were prepared by evacuating the solvent under vacuum at room temperature. UV-Visible absorption spectra were recorded with Cary 50-Bio UV-Visible spectrophotometer. Transmission electron microscopy (TEM) data was obtained using a Technai Spirit G^2 Twin (FEI Company) transmission electron microscope fitted with LaB_6 filament operated at 120kV. Samples were dispersed in hexanes, and then drop cast onto carbon film (20-30 nm) on 200 mesh copper grid (Electron Microscopy Sciences) and allowed to dry in the air. Electron micrographs were obtained by projection onto Gatan US1000 or Orius SC200 CCD Digital Camera and recorded with Digital Micrograph software. The metal content of each sample was determined using ICP-AES elemental analysis (Galbraith Laboratories, Inc.) of calcined samples (450°C, 6 hours in air). XPS data were collected using a Kratos Axis Ultra XPS with a monochromatic Al Kα X-ray source operated at 14 kV, 20 mA in hybrid slot mode. The survey scans were done using a pass energy of 80 eV, with a 0.5 eV step size and 150 ms dwell time. The high resolution scans were done using a pass energy of 20 eV and a step size of 0.1 eV. The high resolution spectra are charge corrected by assigning the C-1s peak to 284.6 eV.

Results and Discussion

The bimetalated nanocrystals were prepared by sequential addition of transition metal ions in two reaction steps. Each transition metal adds to the surface at a characteristic temperature. Thus, for each bimetallic combination, the transition metal that adds at higher temperature must be added in the first step followed by addition of the second metal at lower temperature in the second step. As noted in our earlier work, addition of a transition metal below its optimum temperature leads to poorer yield whereas higher temperature leads to loss of solubility of the nanocrystal and precipitates. The bimetalated nanocrystals are stabilized with oleylamine ligands and disperse in non-polar solvents. They can be easily processed by centrifugation of the dispersion to remove insolubles, then precipitating the nanocrystals with a non-solvent such as ethanol followed by centrifugation to recover the product as a solid. The solid readily redisperses again in non-polar solvent, and the bimetalated nanocrystals can be subject to several cycles of precipitation/redispersion in order to obtain pure surface modified nanocrystals free from extraneous unbound ligands or transition metals.

In our prior work in which we report singly metalated M-TiO_2 NRs, we demonstrate quantitative control of the addition of the transition metal ion to the surface of the nanocrystal. We were able to titrate the surface sites on the TiO_2 nanocrystal such that addition of transition metal ion to the surface occurs in stoichiometric proportion until the surface sites are saturated and no further addition takes place. This is a chemisorption phenomenon in solution, analogous to chemisorption of a gas on a solid. This is, by far, the most convincing evidence that the reaction takes place on the surface of the nanocrystal.

Now, we present two-metal titration experiments in order to prove quantitative adsorption of two

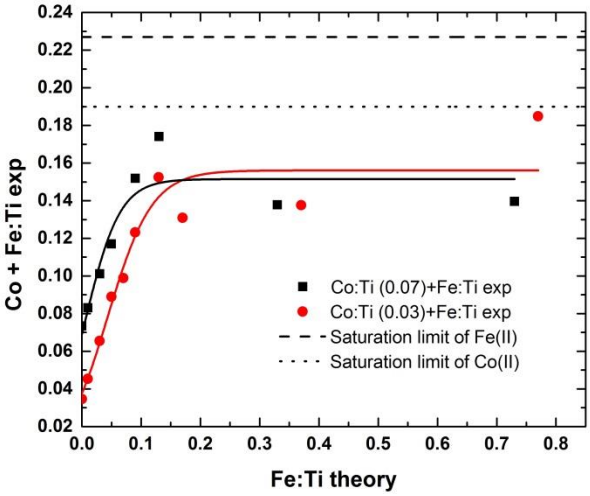

Figure 14. Addition of Fe^{2+} ion to Co-TiO_2 NR with an initial Co:Ti ratio of 0.025 and 0.05.

transition metal ions on the surface of the TiO_2 nanocrystal. In the experiment, Co(II) is added to TiO_2 at a level well-below surface saturation in step 1, then Fe(II) is added to bind to the remaining TiO_2 surface sites in step 2. Thus, we prepared two Co-TiO_2 NR samples with Co:Ti = 0.025 and 0.05. In a second reaction step, Fe^{2+} was added to the Co-TiO_2 NR at a chosen theoretical Fe:Ti ratio. After the reaction, the sample was recovered, calcined, and characterized with elemental analysis for Fe content. A series of reactions in which we conduct step 2 were carried out using either the Co:Ti = 0.025 or 0.05 Co-TiO_2 NR as a starting material. For example, samples in the series Co,Fe-TiO_2 NR with Co:Fe:Ti = 0.025:0.01:1, 0.025:0.03:1, 0.025:0.05:1, 0.025:0.07:1, 0.025:0.1:1, 0.025:0.25:1, and 0.025:0.5:1 requires preparation of Co-TiO_2 NR (0.025:1 Co:Ti) followed by six separate reactions in which step 2 was carried out. In this way, data were acquired *ex-situ* to establish the loading of the second metal ion on the surface of M-TiO_2. In **Figure 14**, results of elemental analyses are plotted as measured [(mol Fe + mol Co)/(mol Ti)] versus theoretical Fe:Ti. **Figure 14** contains two datasets showing the adsorption of Fe onto Co-TiO_2 NR at Co:Ti = 0.025 or 0.05 (black and red points, respectively). Initially, adsorption of Fe to the Co-TiO_2 NR occurs with high yield (slope ≈ 1 for both datasets), then the curve becomes flat indicating no further adsorption. The shape matches a type I Langmuir adsorption isotherm. We demonstrate that saturation of the surface sites with Fe(II) can be achieved at different initial loadings of Co(II). Therefore, a wide range of ratio of M:M' can be selected at loadings up to the saturation point.

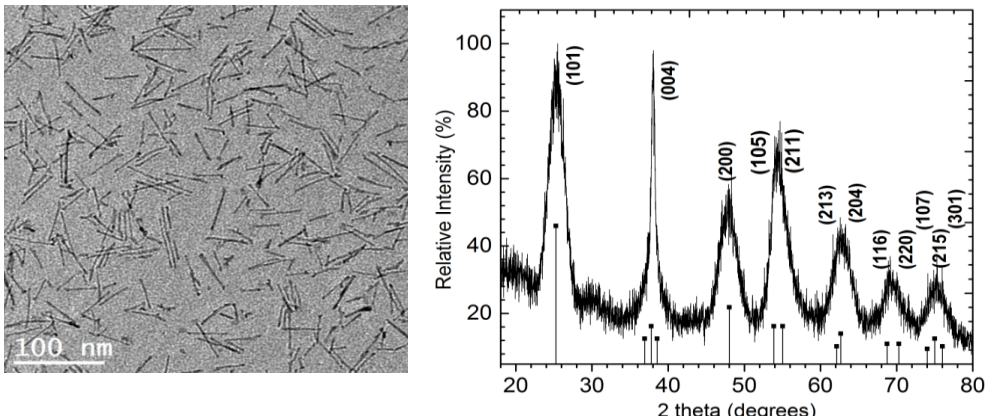

Figure 15. (Left) TEM image of Co,Fe-TiO_2 NRs and (Right) powder X-ray diffraction data of Co,Fe-TiO_2 NRs with JCPDS reference (21-1272) of anatase TiO_2 NRs.

The M,M'-TiO_2 products were characterized with transmission electron microscopy and powder X-ray diffraction (**Figure 15**). The data establish retention of the original TiO_2 nanocrystal phase and morphology upon sequential metalation, no new crystal phases or additional nanoparticulate materials are formed, and that the samples do not aggregate. **Figure 15** (right) shows the powder X-ray diffraction patterns of the as prepared samples. These patterns are well indexed to *anatase* TiO_2. No peaks of metal nanoparticles or metal oxides or other TiO_2 phases are detected.

UV-visible spectra of the samples are presented in **Figure 16**. The spectra largely resemble a

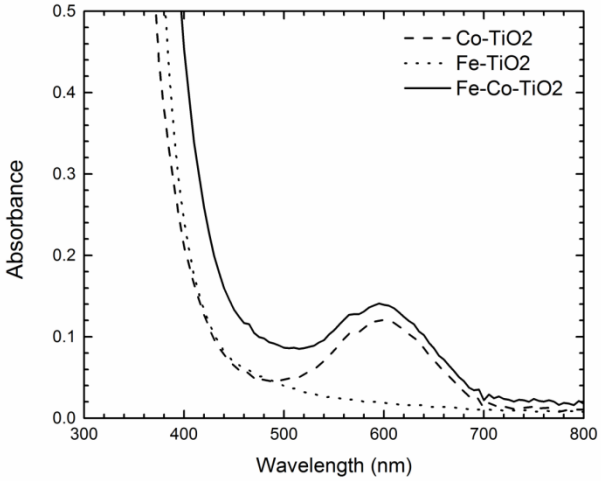

Figure 16. UV-visible spectrum of Co-TiO_2, Fe-TiO_2, and Co,Fe-TiO_2 NRs.

superposition of the absorbance features attributed to each adsorbed transition metal ion. The results suggest little electronic communication exists between the transition metal ions in the bimetalated system. This may not be surprising, given the absorbance features in the singly metalated TiO_2 nanocrystal samples are similar to those of monometallic coordination complexes.

X-ray photoelectron spectroscopy (XPS) experiments were performed for the M,M'-TiO_2 NR samples (**Figure 17**). The XPS data of M-TiO_2 samples were reported previously. The XPS data of the M,M'-TiO_2 nanocrystals indicates the presence of two distinct transition metals in all of the samples. The oxidation states are identical to that found in the M-TiO_2 nanocrystal samples. This indicates that there is no electron transfer between the transition metals and likely that there are not delocalized electronic states that include the transition metals M or M'.

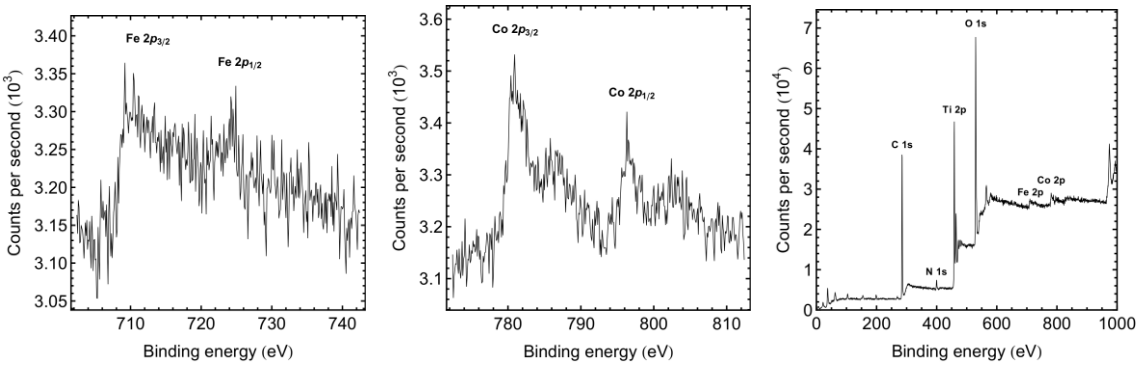

Figure 17. XPS data of Co,Fe-TiO_2 NR showing the Fe 2p region (left), Co 2p region (middle), and full spectrum (right).

Conclusion

We developed a synthetic protocol to form bimetalated M,M'-TiO_2 nanocrystals in which two different first-row transition metal ions were adsorbed to the surface of the nanocrystal with quantitative control of the metal loading and M:M' ratio. We establish that the reaction proceeds with retention of the nanocrystal phase and morphology, and that the reaction occurs on the surface of the nanocrystal. The electronic structure of the materials appears to show no electronic communication between the transition metal ions as delocalized states. We are interested in developing the bimetalated TiO_2 nanocrystals as photocatalysts and to test whether photo-generated excitons can become separated on the two different surface metal sites.

This work has been submitted to *Chemistry of Materials* in October 2014. This manuscript acknowledges FA9550-12-1-0204 for funding. A previous manuscript on singly metallated TiO_2 NRs has been published in *Inorg. Chim. Acta* (422 (2014) 8) and acknowledges AFOSR funding.